



Plasmon-Enhanced Optical Control of Magnetism at the Nanoscale via the Inverse Faraday Effect

Journal Article

Author(s):

Parchenko, Sergii; [Hofhuis, Kevin Anthony](#) ; Larsson, Agne Åberg; Kapaklis, Vassilios; Scagnoli, Valerio; [Heyderman, Laura J.](#) ; Kleibert, Armin

Publication date:

2025-01

Permanent link:

<https://doi.org/10.3929/ethz-b-000678848>

Rights / license:

[Creative Commons Attribution 4.0 International](#)

Originally published in:

Advanced Photonics Research 6(1), <https://doi.org/10.1002/adpr.202400083>

Plasmon-Enhanced Optical Control of Magnetism at the Nanoscale via the Inverse Faraday Effect

Sergii Parchenko,* Kevin Hofhuis, Agne Åberg Larsson, Vassilios Kapaklis, Valerio Scagnoli, Laura Jane Heyderman, and Armin Kleibert*

The relationship between magnetization and light has been the subject of intensive research for the past century. Herein, the impact of magnetization on light polarization is well understood. Conversely, the manipulation of magnetism with polarized light is being investigated to achieve all-optical control of magnetism, driven by potential technological implementation in spintronics. Remarkable discoveries, such as the single-pulse all-optical switching of magnetization in thin films and submicrometer structures, have been reported. However, the demonstration of local optical control of magnetism at the nanoscale has remained elusive. Herein, it is demonstrated that exciting gold nanodiscs with circularly polarized femtosecond laser pulses lead to ultrafast, local, and deterministic control of magnetization in an adjacent magnetic film. This control is achieved by exploiting the magnetic moment generated in plasmonic nanodiscs through the inverse Faraday effect. The results pave the way for light-driven control in nanoscale spintronic devices and provide important insights into the generation of magnetic fields in plasmonic nanostructures.

materials such as electron–electron, electron–spin, and electron–lattice interactions. Importantly, femtosecond laser pulses can be used to rapidly quench the magnetization within a subpicosecond time frame due to ultrafast heating.^[3] Here, the ultrashort laser pulse drives the material to an out-of-equilibrium state by decoupling the spin, electron, and lattice system during the excitation process, inducing ultrafast demagnetization (DM) dynamics.^[4] Another remarkable effect of the interaction of ultrashort pulses with magnetic materials is all-optical switching (AOS) where the magnetization state can be reversed at the picosecond time scale by means of photoexcitation.^[5] Currently, AOS is considered to be primarily driven by heating effects,^[6] and a variety of materials and engineered structures are known to undergo AOS, either as a stochastic multipulse process or single-pulse toggle switching.^[7–9]


Another way to manipulate the magnetization with light is through the inverse Faraday effect (IFE), where circularly polarized light acts as an effective magnetic field that changes the net magnetic moment of the system.^[10,11] The sign of the effective magnetic field associated with light due to the IFE depends only on the handedness of the circular polarization,^[12]

1. Introduction

The manipulation of magnetic states in materials using light has been the subject of intense research for several decades.^[1,2] With the development of high-intensity pulsed light sources, it is now possible to modify the magnetization within time scales comparable to the fundamental electronic interaction times in magnetic

S. Parchenko, K. Hofhuis, V. Scagnoli, L. J. Heyderman
Laboratory for Mesoscopic Systems
Department of Materials
ETH Zurich
8093 Zurich, Switzerland
E-mail: sergii.parchenko@xfel.eu

S. Parchenko, K. Hofhuis, V. Scagnoli, L. J. Heyderman
Laboratory for Multiscale Materials Experiments
Paul Scherrer Institute
5232 Villigen PSI, Switzerland

 The ORCID identification number(s) for the author(s) of this article can be found under <https://doi.org/10.1002/adpr.202400083>.

^[†]Present address: Ericsson Research, Torshamnsgatan 23, 16483 Stockholm, Sweden

© 2024 The Author(s). Advanced Photonics Research published by Wiley-VCH GmbH. This is an open access article under the terms of the Creative Commons Attribution License, which permits use, distribution and reproduction in any medium, provided the original work is properly cited.

DOI: 10.1002/adpr.202400083

S. Parchenko
European XFEL
Holzkoppel 4, 22869 Schenefeld, Germany

K. Hofhuis
Laboratory for Nano and Quantum Technologies
Paul Scherrer Institute
5232 Villigen PSI, Switzerland

A. Å. Larsson,^[†] V. Kapaklis
Department of Physics and Astronomy
Uppsala University
Box 516, 751 20 Uppsala, Sweden

A. Kleibert
Swiss Light Source
Paul Scherrer Institute
5232 Villigen PSI, Switzerland
E-mail: armin.kleibert@psi.ch

hence making it a promising approach for ultrafast optospin-
tronic applications.^[13,14] Indeed, in several studies, it has been
shown that magnetization precession can be triggered by the
IFE,^[12,13,15–17] and the role of the IFE in AOS with single and
multiple pulses is the focus of ongoing theoretical and experi-
mental research.^[7,18–21]

Despite the impressive progress in understanding the interac-
tion of ultrafast laser pulses with magnetic matter and the tech-
nological drive to achieve ultrafast, contactless control of
magnetism, there are important challenges for the implementa-
tion of all-optical magnetization control in real applications. First
of all, for most applications, it will be necessary to address nano-
scale structures that are much smaller than the optical wave-
length of the exciting laser sources.^[22] Indeed, heat-assisted
AOS was demonstrated on the micrometer^[23] and nanometer
scales,^[24,25] but deterministic control of the magnetization on
the nanoscale is yet to be achieved. Another challenge is that
a strong magneto-optical response is typically required to gener-
ate a substantial magnetic moment by the IFE, but achieving this
is not easy because the associated strong optical absorption is
typically unfavorable for the IFE. This is because the IFE field
in metals is generated when the electromagnetic field of the opti-
cal wave acts on the electrons in the medium, inducing electron
motion in the direction of the electric field associated with
incoming illumination.^[26,27] If too many photons are absorbed,
however, the driving force for this effect is suppressed. For this
reason, in previous experimental demonstrations of large ampli-
tude magnetization dynamics driven by the IFE, the focus has
mainly been on inducing this effect in magnetic dielectrics with
strong magneto-optical response while using optical excitation
below the bandgap at low absorption. Thus, achieving IFE-driven
control of magnetization in absorbing media such as metals and
at the nanoscale is an active area of research and development,
with potential benefits for prospective nanoscale devices, includ-
ing lower energy requirements and increased operation speed.

One way to achieve effective control of the magnetization by
light at the nanoscale is to employ plasmonic nanostructures.
These structures can be used to concentrate the electromagnetic
field of incident light down to the nanoscale,^[28,29] resulting in a
higher coupling efficiency to the material near the nanostruc-
tures. This capability opens up new possibilities for achieving
effective control of magnetization at the nanoscale using light.
Moreover, when using circularly polarized light and suitable
geometries, plasmonic nanostructures have been predicted to
generate effective magnetic fields with magnitudes of the order
of one Tesla,^[22,30–32] and recent experimental demonstrations
using plasmonically active gold nanoparticles have generated
transient magnetic moments of $\approx 0.95 \mu_B$ per gold atom.^[33] In
this case, the magnetic moments originate from the motion of
the electrons, which follow the electric field of the incident laser
pulse. However, for technological applications, it is crucial to
understand whether the magnetic moment generated by light
in plasmonic nanostructures can be harnessed to impact the
magnetic moment of the adjacent magnetically ordered sample.

In this study, we employ finite-difference time-domain
(FDTD) simulations in conjunction with two-color pump-probe
experiments to showcase the deterministic and nanoscale manip-
ulation of magnetization within a ferrimagnetic TbCo film coated
with arrays of plasmonic gold nanodisc on the ultrafast timescale.

The experiments presented here are conducted using a single-
excitation wavelength, while precision in modulating the plas-
monic excitation efficiency is achieved by varying the dimensions
of the nanostructures. This approach circumvents potential inter-
ference from the wavelength-dependent optical response of the
material, thus ensuring that plasmon-induced effects remain dis-
cernible. Furthermore, our investigations are carried out on sam-
ples exhibiting a magnetic multidomain state, as opposed to a
uniformly magnetized state. This deliberate choice enables the
suppression of certain non-IFE contributions, facilitating the
unambiguous detection of IFE in both the bare TbCo film
and its gold nanodisc-coated counterpart. Consistent with our
simulations, we observe that the plasmonic IFE-driven control
of the adjacent magnetic medium exhibits greater efficacy in
proximity to the plasmon resonance compared to on-resonant
excitation. Our findings not only pave the way for achieving ultra-
fast magnetism control at the nanoscale, but also underscore that
this control is attainable in metallic systems with low absorption,
mitigating concerns related to sample overheating.

2. Results

2.1. Finite-Difference Time-Domain Simulations

First, we explore the conditions necessary to achieve local IFE
amplification in gold nanodiscs on the magnetic support in
the vicinity of the localized surface plasmon resonance
(LSPR).^[34] Specifically, the system under examination consists
of gold nanodisc arrays with a thickness of 15 nm on top of a
20 nm-thick Tb₂₄Co₇₆ alloy film on a SiO₂ substrate, similar to
the samples under experimental investigation (see Figure 2a–c
and Experimental Section).^[35] The simulations are carried out
for nanodiscs with radius R varying from 30 to 120 nm and
for different excitation wavelengths ranging from $\lambda = 300$ to
1300 nm utilizing FDTD calculations. The simulations consider
circularly polarized light pulses with a duration of 35 fs at per-
pendicular incidence, as schematically shown in the inset of
Figure 1a, and include periodic boundary conditions with
50 nm edge-to-edge spacing between the nanodiscs to mimic
the experimental conditions and the investigated samples
(see Experimental Section for more details). It should be noted
that, although the calculations consider pulsed optical excitation,
they do not take the ultrafast excitation effects such as out-of-
equilibrium conditions and the associated temperature changes
in the electronic, spin, and lattice systems into account.^[4]

The calculated transmission through the sample for a range of
 λ and R reveals that the LSPR resonance depends on λ and R as
expected for metallic nanostructures in the present size range.^[34]
Specifically, we find the onset of resonant LSPR absorption at
about $\lambda = 850$ nm and a nanodisc radius R of 30 nm and an
almost linear trend toward $\lambda = 1300$ nm and $R = 90$ nm for
the resonance (red dashed line). We also find weak collective
plasmon modes at lower wavelengths (indicated by yellow dashed
lines), which we will not further consider in the following.^[36] In
Figure 1b–e, we show the calculated spatial distribution of elec-
tric field E and magnetic field H generated by circularly polarized
light with $\lambda = 1030$ nm for nanodiscs with $R = 50$ and 100 nm,
which give resonant and nonresonant excitation, indicated by

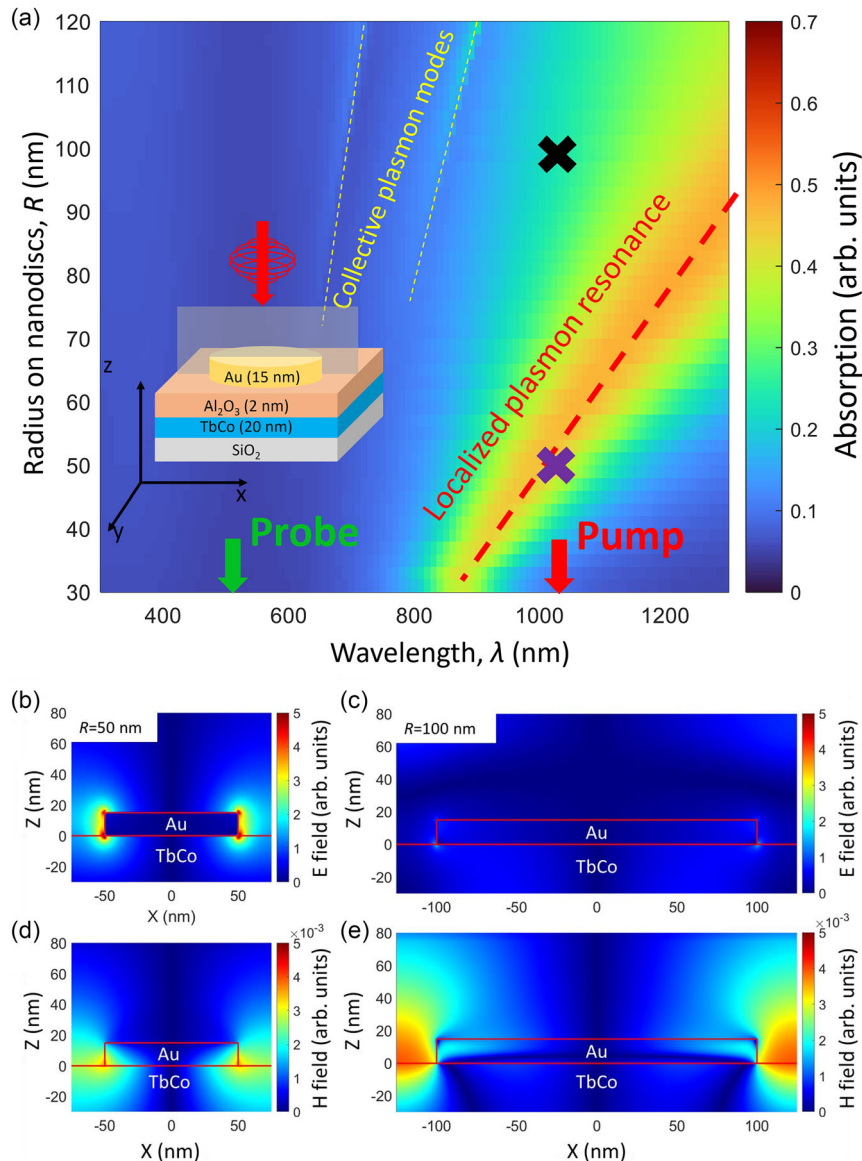


Figure 1. FDTD calculations of LSPR excitation with circularly polarized light. a) 2D map of the absorption as function of the excitation laser wavelength, λ , and the radius of the nanodiscs, R . The red dashed line indicates the LSPR branch. The yellow dashed lines indicate collective plasmonic modes. Purple and black crosses indicate λ and R used in panels (b–e), respectively. The wavelength of the pump and probe laser beams used in the time-resolved experiments are indicated with red and green arrows, respectively. The inset in panel (a) shows the sample geometry used for the calculations and in the experiments below. b–e) Spatial distribution of electric field E (b,c) and magnetic field H (d,e) generated in plasmonic nanodiscs with $R = 50$ nm (b,d) and with $R = 100$ nm (c,e) when excited with circularly polarized light with $\lambda = 1030$ nm.

the purple and the black cross in Figure 1a, respectively. Note that these graphs display the total spatial distribution of the E and H fields in the sample from the incoming light but not the IFE contribution specifically. For $R = 50$ nm, when the optical excitation matches the LSPR mode, we find a strong concentration of the electric field E at the edges of gold nanodiscs (Figure 1b) as well as a concentration of the magnetic field H at the interface between the plasmonic nanodiscs and the magnetic thin film (Figure 1d) as expected for resonant plasmon excitation.^[34] Interestingly, for a nonresonant excitation of the larger nanodiscs with $R = 100$ nm, we find only a very small

concentration of the E field (Figure 1c) but still a sizable enhancement of the H field at the edges of the nanodiscs (Figure 1e). All calculations in Figure 1 are carried out for left-handed polarization, but the results are the same for right-handed polarization.

2.2. Time-Resolved Experiments and Magnetic Domain Configuration of the TbCo Film

In order to address experimentally the LSPR of gold nanodiscs on a magnetic TbCo film and the impact of circularly polarized laser pulses, we perform ultrafast time-resolved investigations using a

two-color pump-probe approach. The samples are lithographically prepared gold nanodisc arrays with R varying from 30 to 100 nm on top of a TbCo film with out-of-plane magnetization on a SiO_2 substrate (see Experimental Section) similar to the sample geometry used in numerical calculations (see inset to Figure 1a). The arrays have lateral dimensions of $300 \times 300 \mu\text{m}$, ensuring that they are larger than the footprint of the laser pulses, which is about $200 \mu\text{m}$ in diameter. Scanning electron microscope micrographs of arrays of nanodiscs with radii $R = 30 \text{ nm}$ and $R = 100 \text{ nm}$ are shown in Figure 2a,b, respectively. The 50 nm edge-to-edge spacing between the neighboring nanodiscs ensures highly dense arrays covering 45–55% of the TbCo film surface depending on the disc radius. Thus, a large proportion of the TbCo film is affected when exciting the nanodiscs, increasing the detectable magnetic signal.

The experimental geometry for the time-resolved experiments is depicted in Figure 2c. Femtosecond laser pulses with circular polarization and $\lambda = 1030 \text{ nm}$ are used for optical excitation and linearly polarized pulses with $\lambda = 515 \text{ nm}$ are used as a probe. Polarization analysis with a balanced photodetector is used to track transient changes in the magnetization of the TbCo film via the Faraday effect, while intensity measurements of the transmitted probe pulses are used to measure the transient absorption of the sample. The pump wavelength and the investigated range of nanodisc radii circumvent the excitation of collective plasmonic modes (see Figure 1a), which could otherwise couple

to the LSPR mode.^[37] Moreover, the probe pulse wavelength is far from the plasmon resonances as shown in Figure 1a, minimizing the effect of the plasmon excitation in the gold nanodiscs on the polarization state of the probe pulse.^[38,39] Furthermore, there is a major challenge to separate magneto-optical contributions from Au discs and TbCo. The magnetic field generated in plasmonic nanodiscs will also magnetize the gold nanodiscs and bring an additional contribution to the measured Faraday rotation signal and both signals are expected to have the same pulse-like shape. However, the reported Kerr magneto-optical response of gold in reflection geometry at our probe wavelength is about 0.67 mdeg/Tesla,^[40] which is two orders of magnitude smaller than the one for TbCo alloy of about 63 mdeg/Tesla.^[41] This assessment relies on comparing the static magneto-optical response of the TbCo and Au film. For the case of nanostructured plasmonic systems and optical excitation with ultrashort laser pulses, this comparison may not be fully applicable due to probing the dynamics in out-of-equilibrium state. Nevertheless, we expect that the rotation of the polarization of the probe beam due to IFE magnetized gold is smaller when compared to that induced by the change of magnetization state in TbCo, and we probe mostly the response of the TbCo film due to the excitation of the gold nanodisc/TbCo film system. In addition, both the excitation and probe beams are incident normal to the sample surface and have a pulse duration of $\approx 250 \text{ fs}$, and the pump fluence during the experiments was kept at $\Phi = 0.5 \text{ mJ cm}^{-2}$ to

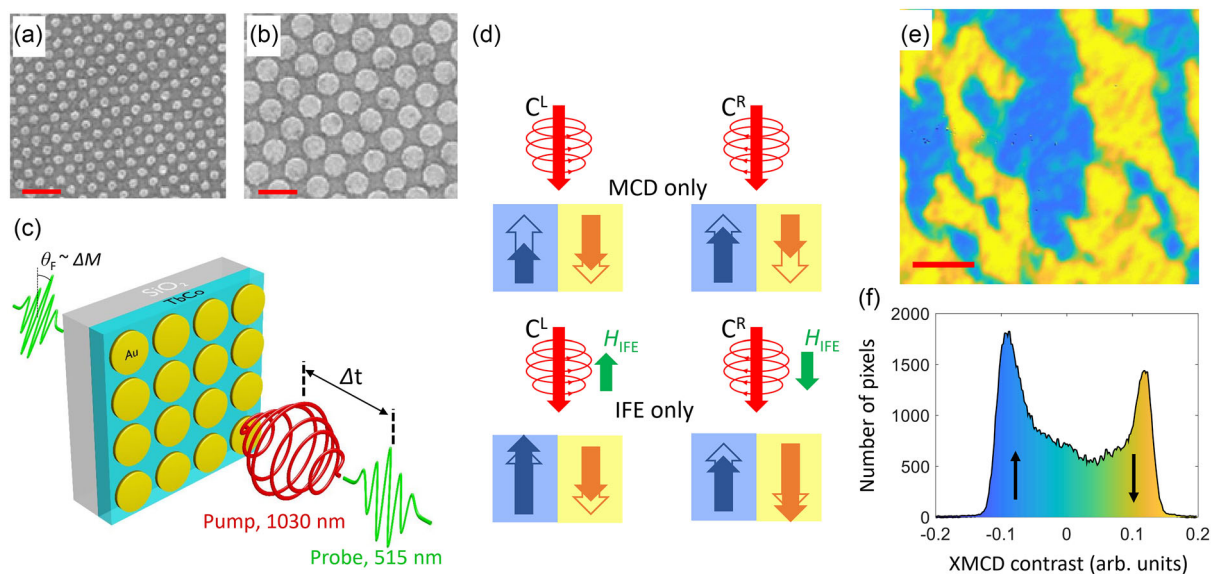


Figure 2. TbCo film with patterned gold nanodiscs and schematics of the time-resolved experiments. a,b) Scanning electron microscope images of Au nanodiscs on top of a TbCo film with $R = 30 \text{ nm}$ and $R = 100 \text{ nm}$, respectively. The red scale bar on both images corresponds to 300 nm . The spacing between neighboring nanodiscs is 50 nm for both arrays. c) Experimental geometry for the time-resolved magnetization dynamics experiments. The sample was excited with a circularly polarized $\lambda = 1030 \text{ nm}$ pump beam and the magnetization change was tracked following the Faraday rotation of a linearly polarized $\lambda = 515 \text{ nm}$ probe beam. d) Schematics indicating the difference between MCD and IFE-related transient modification of the magnetization, ΔM , in magnetic domains with opposite orientation of the magnetic moments. The laser-induced magnetization state is denoted with filled arrows and the equilibrium magnetization state with open arrows. During the MCD effect, the magnetization in domains with opposite orientation is suppressed with different efficiency when pumped with circularly polarized pulses, while the IFE causes modification of the magnetic state that is only related to the helicity of the circularly polarized pump and is equal in magnetic domains with opposite orientation of magnetization. e) A representative magnetic domain configuration in the TbCo film was visualized taking advantage of the XMCD effect at the Co L_3 edge recorded by means of X-ray photoemission electron microscopy. Blue and yellow domains correspond to regions with the magnetization pointing upwards or downwards, respectively. The red scale bar corresponds to $2 \mu\text{m}$. f) Histogram of the XMCD contrast values derived from the magnetic contrast map in panel (e).

prevent damage to the nanostructures, which would occur at higher fluences. The experiments were conducted in the absence of an external magnetic field. More information on the experimental procedure is available in the Experimental Section.

In order to detect the LSPR-enhanced effect of IFE on the magnetic state of the sample, we have chosen a magnetic configuration, that differs from that used in most investigations on ultrafast magnetization dynamics, which are typically carried out on uniformly magnetized samples. In the latter case, the absorption of the pump pulse leads to a dominant signal due to ultrafast DM, which may mask the IFE. Furthermore, when using circularly polarized light pulses, the absorption and the associated DM become polarization dependent due to the magnetic circular dichroism (MCD) effect, which presents an additional challenge to isolate the IFE contributions from the measured signal.^[42] In order to overcome these difficulties, we perform the experiments on a TbCo sample with nearly equal amounts of M_{up} and M_{down} domains. The DM process in the absence of MCD for such a configuration occurs simultaneously in both types of domains and, hence, the integrated Faraday rotation experienced by the probe pulse remains zero at all times. Also, when taking the MCD effect into account, the DM averaged over both types of domains is the same for both polarizations, C^{L} and C^{R} , respectively, and hence, the Faraday rotation averaged over a multidomain sample remains again zero at all times (Figure 2d upper panel). It should be noted that the dynamics and efficiency of the laser-induced DM are expected to be the same in both single and multidomain states. In contrast, the IFE will generate the same transient ΔM in the excited sample region independent of the local domain orientation, M_{up} or M_{down} , with its sign depending only on the polarization of the pump pulse (Figure 2d lower panel).

The actual domain configuration of the investigated TbCo film is shown in Figure 2e and is obtained by combining X-ray MCD (XMCD) at the Co L_3 edge with X-ray photoemission electron microscopy (see Experimental Section for more information about the experimental procedure). The image reveals irregular domains with magnetization pointing up (in blue) and down (in yellow). The typical domain size is of the order of several micrometers, and hence much smaller than the pump and probe laser spot footprint, so avoiding the situation where large magnetic domains would result in a dominant DM and MCD effects is important. However, a detailed statistical analysis of the image pixels shows a smaller imbalance in M_{up} and M_{down} , which is likely to be due to pinning effects (Figure 2f). It should also be noted that, while the gold nanodiscs do not appear in the magnetic contrast images, we observed no spatial correlation between the magnetic domains and the gold nanodisc arrays. Also, measurements in a multidomain state require materials with a high coercive field to ensure that the domain pattern is not redistributed after each laser shot (see data in Figure S2, Supporting Information).

2.3. Two-Color Pump-Probe Investigations

Figure 3a shows the transient transmittance change ΔT , measured at the probe wavelength for the sample covered with a gold nanodisc array ($R = 50$ nm) and for both pump-pulse

polarizations, C^{R} and C^{L} , which reflect the dynamic changes in the nonmagnetic, optical properties of the sample arising from the excitation of the electronic system. Notably, the absence of polarization dependence is noteworthy and corresponds to what is anticipated in a multidomain state, where the MCD effect cancels out. The peak change in transmission, ΔT^{max} , is observed at a delay time of around 0.2 ps and is directly proportional to the absorption of the sample. Figure 3b shows ΔT^{max} as a function of nanodiscs radius, normalized to its value for $R = 30$ nm (black squares), and exhibits a dependence, consistent with the computed absorption (red line) obtained from the FDTD calculations described earlier. Experimentally, the maximum absorption is identified at $R = 60$ nm, aligning with the predicted LSRP at the pump wavelength in our specific samples.

Figure 3c showcases the pump-induced Faraday rotation in the probe beam, that is, the transient change in magnetization, ΔM , for a sample covered with 50 nm gold nanodiscs, while Figure 3d presents the same for the bare TbCo film for comparison. In both cases, a distinct helicity-dependent evolution of ΔM is observed on top of a time-dependent signature resembling the characteristic signal of thermally induced DM, peaking a few hundred femtoseconds after the pump pulse. Notably, the data highlight a more pronounced polarization dependency in the nanodisc-decorated portion of the sample compared to the bare TbCo film. Note that, in both Figure 3c,d, the time traces measured after excitation with opposite circular polarization display no difference between the ΔM signal at late delay times, further confirming the absence of MCD contribution to the measured signal. At the same time, excitation with linear polarization fits in between time traces after excitation with circular polarization (see Figure S1, Supporting Information).

For further analysis, we separate the IFE-related change of the magnetization ΔM_{IFE} and the DM component ΔM_{DM} as follows.

$$\Delta M_{\text{IFE}}(t) = \Delta M_{\text{C}^{\text{L}}}(t) - \Delta M_{\text{C}^{\text{R}}}(t) \quad (1)$$

$$\Delta M_{\text{DM}}(t) = \Delta M_{\text{C}^{\text{L}}}(t) + \Delta M_{\text{C}^{\text{R}}}(t) \quad (2)$$

where $\Delta M_{\text{C}^{\text{L}}}(t)$ and $\Delta M_{\text{C}^{\text{R}}}(t)$ are the time-resolved signals when pumped with left- and right-handed circular polarization, respectively. The respective data are plotted in Figure 3e,f. Figure 3e includes for comparison the data for a 100 nm gold nanodisc sample, which reveals similar dynamics, but different amplitudes of ΔM_{DM} and ΔM_{IFE} compared to the sample with 50 nm gold nanodiscs. The pulse-like shape of the ΔM_{IFE} signal, having a width of ≈ 300 fs which is comparable to the pulse duration, is as expected for an IFE-driven magnetization change.^[43] Comparing the data in Figure 3c,e with the bare TbCo film in Figure 3d,f, shows that the IFE-related modification of magnetization in TbCo is much stronger when the gold nanodiscs are present. However, the IFE peak position in bare TbCo is shifted in time compared to time zero, which is unexpected as the IFE is expected to occur during pump excitation. The IFE-driven magnetization change in the TbCo film is due to the transfer of angular momentum from light to electrons. With a 515 nm probe, we are mostly sensitive to the magnetization of the Tb sublattice that consists of magnetic moments associated with localized $4f$ electrons and delocalized $5d$ electrons.^[44–46] At the same time, optical excitation with 1030 nm at the first instance is absorbed by $3d$

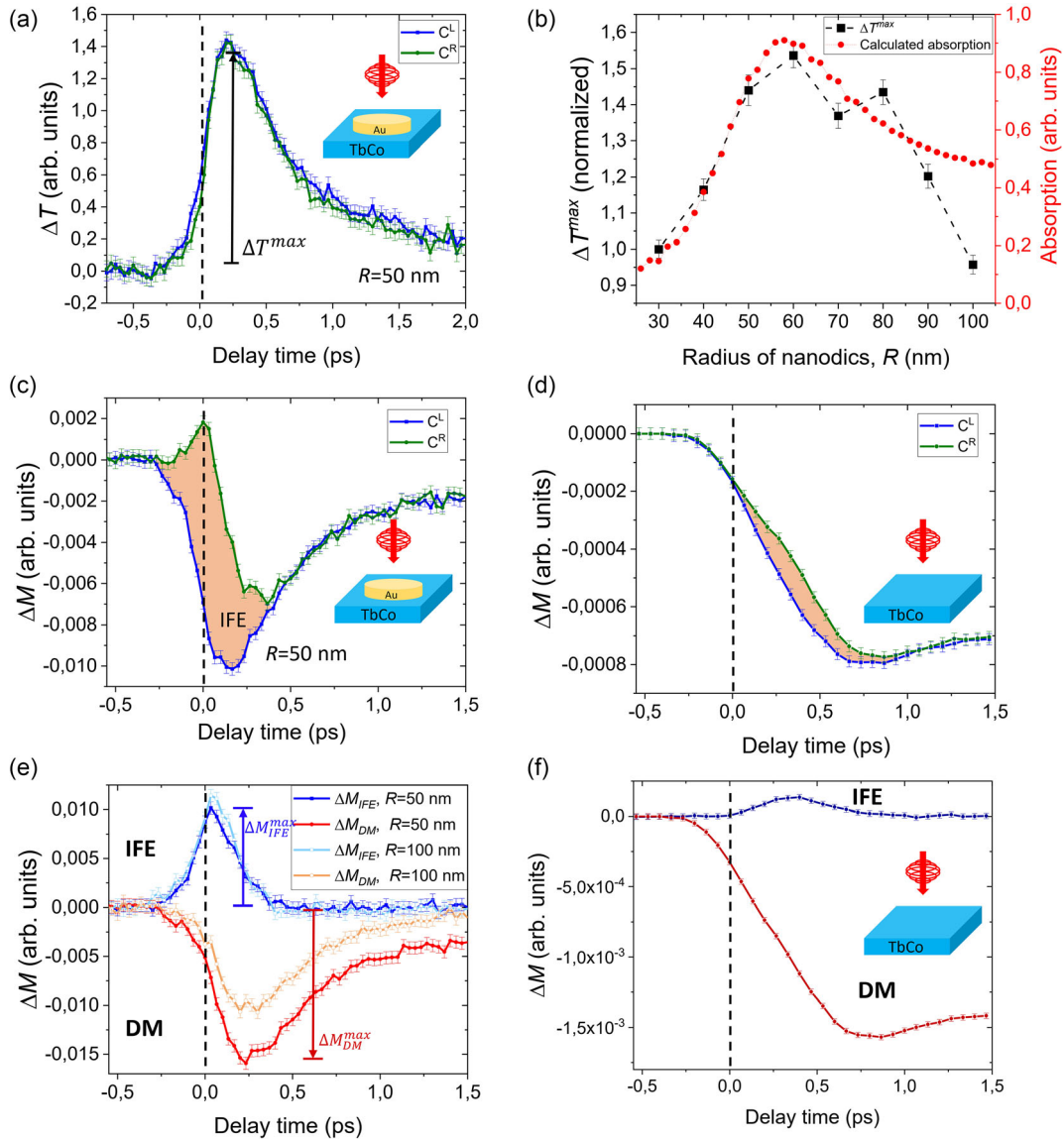


Figure 3. Magnetization dynamics following laser excitation of TbCo in the presence of gold plasmonic structures. a) Transient transmittance signal after the pump excites the part of the sample with arrays of gold nanodiscs with $R = 50$ nm and probed with 515 nm light. b) Comparison of maximum pump-induced transmittance changes ΔT^{\max} as a function of the radius of nanodiscs, R , and calculated absorption. The data for ΔT^{\max} is normalized to its value for $R = 30$ nm. c,d) Time-resolved magnetization change after the pump excites the part of the sample with arrays of gold nanodiscs with $R = 50$ nm and the bare TbCo film, respectively. The difference between traces measured after excitation with opposite circular polarization of pump light is due to the IFE (indicated with an orange shaded area). e) IFE and DM components of the magnetization change, ΔM , for nanodiscs with $R = 50$ nm and $R = 100$ nm. IFE and DM contributions have different amplitudes for nanodiscs with different radii. The maximum values of each component discussed in the text are indicated. The width of the IFE contribution is ≈ 300 fs which is comparable to the pulse duration. f) IFE and DM components for bare TbCo film. Note that the maximum of ΔM_{IFE} occurs at a later time delay compared to nanostructures.

electrons of Co and $5d$ electrons of Tb. Only later the excitation is transferred from $5d$ to $4f$ electrons of Tb which contributes mostly to magneto-optical signals at 515 nm. Simultaneously there is an exchange of angular momentum between Co and Tb after laser excitation that is responsible for all-optical magnetization reversal in rare earth-transition metal alloys.^[6] The combination of these two processes, in our opinion, causes the delay of the IFE signal for bare film and also indirectly confirms that the amplification of the IFE effect in the case of Au/TbCo system

comes from the nanodiscs itself but not in the TbCo film, as the effect in case of Au/TbCo system is instant with pump pulse.

3. Discussion

In the present experiments, the plasmon-assisted optical modification of the magnetic state in the thin-film/nanodisc system following optical excitation involves three distinct contributions.

1) The polarization-independent signal ΔM_{DM} exhibits a signature indicative of a pulse-induced ultrafast DM process. This signal is discernable in our experiments due to the slight imbalance between M_{up} and M_{down} , as discussed above. The size-dependent behavior of the maximum DM ΔM_{DM}^{max} , shown in **Figure 4a**, reflects the resonant absorption of the pump pulses and the associated heating due to the concentrated electric field in the CoTb film near the gold nanodisc edges as expected from ΔT^{max} and the FDTD calculations (see **Figure 3b**).

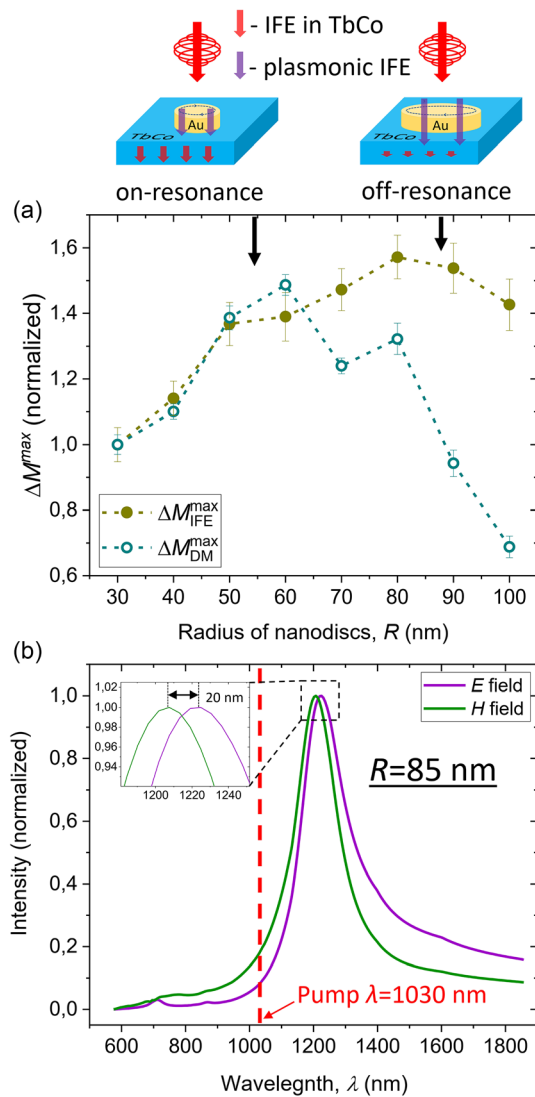


Figure 4. Comparison of different components of the magnetic signal as a function of nanodisc radius and wavelength. a) Maximum of ΔM_{IFE} and ΔM_{DM} components of the laser-induced magnetization change as a function of the radius of nanodiscs, R , obtained from time-resolved experiments. The data are normalized to their value for $R=30$ nm for better presentation. The schematics above panel (a) indicate the different contributions to the ΔM_{IFE} signal for nanostructures with different radii. Purple and red arrows represent the contributions from the plasmonic IFE and the IFE in the TbCo film, respectively. b) Normalized spectral dependence of E and H field for nanodiscs with $R=85$ nm, calculated with FDTD method. The red dashed line indicates the pump wavelength.

The polarization-dependent signal ΔM_{IFE} reflects the IFE-driven impact on the magnetization of the TbCo. This effect is a composite of 2) ordinary IFE in the TbCo film (**Figure 3f**) and 3) plasmonic IFE in the gold nanodiscs. We distinguish two mechanisms of how the plasmonic nanodiscs may affect the magnetization of TbCo: 1) the magnetic field generated in Au nanodiscs directly affects the magnetic state of TbCo and 2) injection of spin-polarized electrons from Au to TbCo film changes the magnetization. We consider the first mechanism as the dominant one as an Al_2O_3 protective layer on top of TbCo film would prevent the spin transfer from gold to the magnetic film.^[47]

Conventionally, plasmon-assisted light-matter interaction is thought to be influenced by the concentration of the electric field of incident light at the nanostructures, leading to increased absorption under plasmon resonance conditions. However, unlike ΔM_{DM}^{max} , ΔM_{IFE}^{max} does not adhere to the radii-dependent absorption profile; it remains elevated, even at larger radii. Note, that the contribution from IFE in the TbCo film to the ΔM_{IFE} signal is still expected to follow the radii-dependent absorption profile because its efficiency linearly depends on the absorbed power (see **Figure S2a**, Supporting Information). Thus, the discrepancy mentioned above must originate from the plasmonic IFE contribution. The schematics above **Figure 4a** illustrate the amplitude of the different contributions to the ΔM_{IFE} signal when pumping nanodiscs with different radii, with the IFE in TbCo and plasmonic IFE represented by red and purple arrows. This experimentally observed difference can be clarified by examining the spectral dependence of E and H fields, which were calculated for a nanodisc with $R=85$ nm (refer to **Figure 4b**). It is essential to note that directly comparing the radius-dependent distribution of E and H at a constant wavelength proves challenging due to normalization issues arising from the equal spacing between nanodiscs, resulting in different areas included in calculations. The spectral evolution of these two fields demonstrates distinct shapes, with the maximum positions shifted by ≈ 20 nm relative to each other. Specifically, at the pump wavelength of 1030 nm, the relative intensity of the H field surpasses that of the E field, exerting a considerable influence on magnetization under nonresonant conditions. A similar trend emerged when analyzing the spectral dependence of E and H field distributions calculated for various radii, yet the most significant difference was observed for nanodiscs with $R=85$ nm.

Despite the strongest photon-plasmon coupling occurring at the LSPR, the efficiency of plasmonic IFE generation is impeded by pronounced optical absorption. The generation of IFE in metals is propelled by electron dynamics that track the electric field of incident light. When an electron absorbs a photon, two key effects ensue: 1) the electric field value diminishes and 2) the thermal energy of the electron increases, potentially rendering it less responsive to the driving force of the incident light's electric field. Both of these processes contribute to the suppression of IFE in highly absorptive media. In contrast, our findings suggest that altering the excitation wavelength slightly away from the plasmon resonance, where absorption increases less, may augment the efficiency of plasmonic IFE. The described processes can be partially analogized to the spectral dependence of IFE in metals. Notably, calculations have demonstrated that the highest efficiency of IFE in metals is anticipated at the photon energies of excitation light where absorption is minimized.^[48]

Furthermore, it is worth comparing the findings reported here with the study on Au nanoparticles from ref. [33]. The IFE description is very often based on a comparison of magneto-optical constants of the direct and IFE. In materials, a maximal IFE is expected in the spectral region with high direct Faraday effect. In Figure 2 of ref. [33], the maximum of direct Faraday effect is observed below plasmon resonance. This is very similar to our observation for $R = 100$ nm where we also see the max plasmonic IFE effect action on TbCo film below the plasma resonance. Hence, the arguments regarding the correlation between direct and IFE in materials could be also extended to the description of plasmonic IFE.

Furthermore, as explained in the Experimental Section, the ΔM value used to present the time evolution of the magnetization state could not be normalized to the saturation magnetization due to the fact that the TbCo film is in a multidomain configuration. Thus, we can only approximately estimate the IFE-related magnetization change. In order to estimate the efficiency of DM after excitation with a laser fluence of 0.5 mJ cm^{-2} , we used a $\text{Tb}_{26}\text{Co}_{74}$ sample with identical geometry but slightly different concentration and, thus, a smaller coercive field ($H_C = 250$ mT) that could be saturated with the applied magnetic field in our setup (see Supplementary Information). In our experiments, with pump fluence of 0.5 mJ cm^{-2} , we suppress about 5% of magnetization if the wavelength of the laser pump is not at the plasmon resonance of the Au nanodiscs with $R = 100$ nm or for a bare TbCo film. This agrees with previous experimental works on ultrafast magnetization experiments in TbCo.^[49–51] Furthermore, in a multidomain state, the magneto-optical sensitivity is proportional to the imbalance of the “up” and “down” domains. The imbalance of magnetization determined from data in Figure 2f is about 8%. Furthermore, for $R = 100$ nm, we have roughly the same magnitudes of ΔM_{DM} and ΔM_{IFE} components, meaning that the change of the magnetization state due to plasmonic IFE is on the order of 0.5% of M at equilibrium. Following the same arguments, we can estimate the IFE in the bare film. The ΔM_{IFE} signal is ≈ 10 times weaker compared to the ΔM_{DM} signal in the TbCo film without nanodiscs. This means that the IFE-driven modification of magnetization in TbCo is about 0.05% of M . This provides a very tentative estimate of the extent of the plasmonic IFE action in a TbCo film, particularly considering the uncertainty in determining the exact contributions of the probed signals and must be taken with care. However, even at this stage, we can conclude that the plasmonic IFE effect surpasses that of regular IFE in TbCo by about an order of magnitude.

4. Conclusion

In summary, we have demonstrated that plasmonic nanostructures can be exploited to increase the optomagnetic response and control the magnetization state of the adjacent media through the plasmonic IFE in a way that can be controlled by light polarization. This opens up new possibilities for the manipulation and control of magnetic materials using light, which has numerous implications for the development of next-generation data storage, data processing, and sensing devices. The observation that plasmonic nanostructures can be used to control the

magnetization, even when the conditions for plasmon resonance excitation are not perfectly met and could be related to different spectral dependencies of plasmon-related absorption increase and plasmonic IFE. Specifically, off-resonant plasmon excitation provides a means to efficiently generate a magnetic field while avoiding a significant increase in absorption, which is a major advantage for heat-sensitive applications. For example, there are several approaches proposed to manipulate the state of quantum systems that rely on the effective magnetic field generated by light for controlling superconducting quantum bits^[52,53] and for controlling photonic networks that operate on neuromorphic principles.^[54] Here, a minimization of absorption to avoid decoherence would be highly beneficial. The striking observation that plasmonic IFE is significant even away from the plasmon resonance implies that further unexpected plasmon-related effects might be discovered when conditions for plasmon resonance excitation are not perfectly met. Such unexpected phenomena would lead the way to novel applications involving the optical control of quantum states on the nanoscale. At the same time, following the discussion in Results, this work also indicates further challenges that must be addressed when revealing the action of plasmonic IFE on adjacent material. The plasmonic antenna and magnetic media are expected to have the same pulse-like shape temporal response. Thus, in the future, it will be important to find the methods to directly separate the effect of the plasmonic IFE on the magnetization from the contribution associated with the plasmonic antenna itself.

5. Experimental Section

Sample Preparation: The sample consisted of a set of several $300 \times 300 \mu\text{m}$ arrays of gold nanodiscs with different radii on top of a TbCo film. An amorphous 20 nm-thick film with a nominal composition of $\text{Tb}_{24}\text{Co}_{76}$ was sputter-deposited with a DC magnetron using Tb and Co targets in an argon atmosphere onto a SiO_2 substrate. A 2 nm-thick Al_2O_3 capping layer was deposited on top of the TbCo film to prevent oxidation. The thin-film preparation method, as well as the structural and magnetic characterization, are described in detail in ref. [35]. TbCo is a ferrimagnetic alloy with two antiparallel magnetic sublattices consisting of Tb and Co atoms. For the given concentration of magnetic elements, the film had an out-of-plane magnetic anisotropy with a coercive field around $H_C = 800$ mT. This relatively high H_C was favorable for our experiments as the magnetic domain structure was more robust to optical excitation. Arrays of gold nanodiscs with radii varying from $R = 30$ nm to $R = 100$ nm, and with a thickness of 15 nm, were prepared using electron beam lithography and thermal evaporation with subsequent lift-off.

FDTD Calculations: Numerical calculations of the optical response of plasmonic nanodiscs were performed with the Ansys Lumerical FDTD software. The structure used in the calculations reflected the actual sample geometry of TbCo (20 nm)/ Al_2O_3 (2 nm)/ Au nanodisc (15 nm). The magneto-optical properties of the $\text{Tb}_{24}\text{Co}_{76}$ alloy film, that is, the polarization- and magnetization-dependent modification of the refractive index, were not taken into account. A schematic of the system geometry used for the calculations is shown in the inset of Figure 1a. The source of circularly polarized light was obtained from a combination of two sources of linearly polarized light with orthogonal polarization direction and a phase shift of $\pi/2$. We used Bloch boundary conditions in the x - and y -directions, which were perpendicular to the propagation direction of the circularly polarized light. Along the z -direction, which is parallel to the propagation direction of the light, we used perfectly matching layer boundary conditions. The cell size was chosen to be $2 \times 2 \times 2 \text{ nm}^3$.

XPEEM Characterization: Magnetic domain imaging was carried out at the Surface/Interface: Microscopy beamline at the Swiss Light Source

using the PEEM end station. Magnetic contrast was extracted using the XMCD effect by taking the asymmetry between two photoemission electron microscopy images recorded with left and right circularly polarized X-rays with the photon energy set to $E = 779$ eV, which corresponded to the Co L_3 absorption edge.

Time-Resolved Experiments: Optical pump-probe experiments to determine the magnetization dynamics were performed in transmittance (Faraday) geometry. Ultrashort laser pulses were generated with an ActiveFiber Yb pulsed fiber laser with a 200 kHz repetition rate and a fundamental wavelength of $\lambda = 1030$ nm. The wavelength of the optical pump was $\lambda = 1030$ nm with circular polarization. Linearly polarized probe pulses with $\lambda = 515$ nm were obtained by frequency doubling using a beta barium borate nonlinear crystal. The pump beam was focused to a spot size of 200 μm and the probe beam size was about 150 μm . Both beams propagated collinearly and impinged on the sample at the normal incidence. The pump fluence was 0.5 mJ cm^{-2} and the probe beam fluence was about 1/50 of the pump fluence. Transient Faraday rotation and transmission of the probe beam were measured with a balanced detection scheme using a Zurich Instruments digital lock-in amplifier. Note that the transient magnetization change ΔM , which is proportional to the Faraday rotation, is given in arbitrary units but not relative to the saturation magnetization. Normalization of the ΔM to the saturation magnetization M was not possible for experiments performed on a sample in a multi-domain state. Our study is based on comparing the time evolution of the magnetic signal obtained when pumping nanodiscs of different radii but with the same spatial separation. This means that the area of the TbCo film covered with plasmonic nanodiscs of different radii varies and the fraction of the probed area varies with the radius of the nanodiscs. In order to compensate for this, we corrected the time traces to the fraction of the sample surface covered by nanostructures. We used several dichroic mirrors and bandpass filters to suppress any pump light signal and to make sure that only the probe pulse was detected.

Supporting Information

Supporting Information is available from the Wiley Online Library or from the author.

Acknowledgements

The authors gratefully thank Anja Weber, Paul Scherrer Institute, for her support during the preparation of nanostructures. K.H. and L.H. acknowledge funding from the Swiss National Science Foundation (project no. 200020_172774). This work was part of a project which received funding from the European Union's Horizon 2020 research and innovation program under grant agreement no. 737093 "FEMTOTERABYTE". The authors gratefully acknowledge the support of the COST Action CA17123 MAGNETOFON.

Open Access funding enabled and organized by Projekt DEAL.

Conflict of Interest

The authors declare no conflict of interest.

Author Contributions

S.P. and A.K. conceived the research. A.A.L. and V.K. deposited the TbCo film. K.H. prepared the gold nanostructures. S.P. performed time-resolved experiments with support from V.S. S.P. performed numerical calculations. S.P. and A.K. performed the X-ray characterization. S.P. wrote the manuscript with the help of A.K. and L.H., with contributions from all coauthors.

Data Availability Statement

The data that support the findings of this study are available from the corresponding author upon reasonable request.

Keywords

inverse Faraday effect, magnetization control, nanoplasmonics, ultrafast dynamics

Received: May 14, 2024

Published online: June 17, 2024

- [1] A. Kirilyuk, A. V. Kimel, T. Rasing, *Rev. Mod. Phys.* **2010**, *82*, 2731.
- [2] A. Kirilyuk, A. V. Kimel, T. Rasing, *Rep. Prog. Phys.* **2013**, *76*, 026501.
- [3] E. Beaurepaire, J.-C. Merle, A. Daunois, J.-Y. Bigot, *Phys. Rev. Lett.* **1996**, *76*, 4250.
- [4] B. Koopmans, G. Malinowski, F. Dalla Longa, D. Steiauf, M. Fähnle, T. Roth, M. Cinchetti, M. Aeschlimann, *Nat. Mater.* **2010**, *9*, 259.
- [5] R. Srikanand, H. Chand, P. Petitjean, B. Aracil, *Phys. Rev. Lett.* **2007**, *99*, 239002.
- [6] T. A. Ostler, J. Barker, R. F. L. Evans, R. W. Chantrell, U. Atxitia, O. Chubykalo-Fesenko, S. El Moussaoui, L. Le Guyader, E. Mengotti, L. J. Heyderman, F. Nolting, A. Tsukamoto, A. Itoh, D. Afanasiev, B. A. Ivanov, A. M. Kalashnikova, K. Vahaplar, J. Mentink, A. Kirilyuk, T. Rasing, A. V. Kimel, *Nat. Commun.* **2012**, *3*, 666.
- [7] C.-H. Lambert, S. Mangin, B. S. D. C. S. Varaprasad, Y. K. Takahashi, M. Hehn, M. Cinchetti, G. Malinowski, K. Hono, Y. Fainman, M. Aeschlimann, E. E. Fullerton, *Science* **2014**, *345*, 1337.
- [8] S. Mangin, M. Gottwald, C.-H. Lambert, D. Steil, V. Uhlir, L. Pang, M. Hehn, S. Alebrand, M. Cinchetti, G. Malinowski, Y. Fainman, M. Aeschlimann, E. E. Fullerton, *Nat. Mater.* **2014**, *13*, 286.
- [9] K. T. Yamada, A. V. Kimel, K. H. Prabhakara, S. Ruta, T. Li, F. Ando, S. Semin, T. Ono, A. Kirilyuk, T. Rasing, *Front. Nanotechnol.* **2022**, *4*, 765848.
- [10] J. P. van der Ziel, P. S. Pershan, L. D. Malmstrom, *Phys. Rev. Lett.* **1965**, *15*, 190.
- [11] L. P. Pitaevskii, *Sov. Phys. JETP* **1961**, *12*, 1008.
- [12] A. V. Kimel, A. Kirilyuk, P. A. Usachev, R. V. Pisarev, A. M. Balbashov, T. Rasing, *Nature* **2005**, *435*, 655.
- [13] A. V. Kimel, M. Li, *Nat. Rev. Mater.* **2019**, *4*, 189.
- [14] M. L. M. Lalieu, R. Lavrijsen, B. Koopmans, *Nat. Commun.* **2019**, *10*, 110.
- [15] S. Parchenko, A. Stupakiewicz, I. Yoshimine, T. Satoh, A. Maziewski, *Appl. Phys. Lett.* **2013**, *103*, 172402.
- [16] G.-M. Choi, A. Schleife, D. G. Cahill, *Nat. Commun.* **2017**, *8*, 15085.
- [17] T. Satoh, Y. Terui, R. Moriya, B. A. Ivanov, K. Ando, E. Saitoh, T. Shimura, K. Kuroda, *Nat. Photon.* **2012**, *6*, 662.
- [18] M. Battiato, G. Barbalinardo, P. M. Oppeneer, *Phys. Rev. B* **2014**, *89*, 014413.
- [19] V. Raposo, R. Guedas, F. García-Sánchez, M. A. Hernández, M. Zazo, E. Martínez, *Appl. Sci.* **2020**, *10*, 1307.
- [20] G. Kichin, M. Hehn, J. Gorchon, G. Malinowski, J. Hohlfeld, S. Mangin, *Phys. Rev. Appl.* **2019**, *12*, 024019.
- [21] F. Cheng, Z. Du, X. Wang, Z. Cai, L. Li, C. Wang, A. Benabbas, P. Champion, N. Sun, L. Pan, Y. Liu, *Adv. Opt. Mater.* **2020**, *8*, 2000379.
- [22] T. M. Savchenko, M. Buzzi, L. Howald, S. Ruta, J. Vijayakumar, M. Timm, D. Bracher, S. Saha, P. M. Derlet, A. Béché, J. Verbeeck, R. W. Chantrell, C. A. F. Vaz, F. Nolting, A. Kleibert, *Phys. Rev. B* **2020**, *102*, 205418.

- [23] L. Le Guyader, M. Savoini, S. El Moussaoui, M. Buzzi, A. Tsukamoto, A. Itoh, A. Kirilyuk, T. Rasing, A. V. Kimel, F. Nolting, *Nat. Commun.* **2015**, *6*, 5839.
- [24] T.-M. Liu, T. Wang, A. H. Reid, M. Savoini, X. Wu, B. Koene, P. Granitzka, C. E. Graves, D. J. Higley, Z. Chen, G. Razinskas, M. Hantschmann, A. Scherz, J. Stöhr, A. Tsukamoto, B. Hecht, A. V. Kimel, A. Kirilyuk, T. Rasing, H. A. Dürr, *Nano Lett.* **2015**, *15*, 6862.
- [25] M. Vergès, S. Perumbilavil, J. Hohlfeld, F. Freire-Fernández, Y. Le Guen, N. Kuznetsov, F. Montaigne, G. Malinowski, D. Lacour, M. Hehn, S. Van Dijken, S. Mangin, *Adv. Sci.* **2023**, *10*, 2204683.
- [26] J. Hurst, P. M. Oppeneer, G. Manfredi, P.-A. Hervieux, *Phys. Rev. B* **2018**, *98*, 134439.
- [27] R. Sinha-Roy, J. Hurst, G. Manfredi, P.-A. Hervieux, *ACS Photonics* **2020**, *7*, 2429.
- [28] S. Kim, T.-I. Jeong, J. Park, M. F. Ciappina, S. Kim, *Nanophotonics* **2022**, *11*, 2393.
- [29] N. Maccaferri, I. Zubritskaya, I. Razdolski, I.-A. Chioar, V. Belotelov, V. Kapaklis, P. M. Oppeneer, A. Dmitriev, *J. Appl. Phys.* **2020**, *127*, 080903.
- [30] X. Yang, Y. Mou, B. Gallas, A. Maitre, L. Coolen, M. Mivelle, *ACS Nano* **2022**, *16*, 386.
- [31] V. Karakhanyan, C. Eustache, Y. Lefier, T. Grosjean, *OSA Continuum* **2021**, *4*, 1598.
- [32] V. Karakhanyan, Y. Lefier, C. Eustache, T. Grosjean, *Opt. Lett.* **2021**, *46*, 613.
- [33] O. H.-C. Cheng, D. H. Son, M. Sheldon, *Nat. Photonics* **2020**, *14*, 365.
- [34] I. Zorić, M. Zäch, B. Kasemo, C. Langhammer, *ACS Nano* **2011**, *5*, 2535.
- [35] A. Ciuculkaite, K. Mishra, M. V. Moro, I.-A. Chioar, R. M. Rowan-Robinson, S. Parchenko, A. Kleibert, B. Lindgren, G. Andersson, C. S. Davies, A. Kimel, M. Berritta, P. M. Oppeneer, A. Kirilyuk, V. Kapaklis, *Phys. Rev. Mater.* **2020**, *4*, 104418.
- [36] G. Baffou, P. Berto, E. Bermúdez Ureña, R. Quidant, S. Monneret, J. Polleux, H. Rigneault, *ACS Nano* **2013**, *7*, 6478.
- [37] K. Mishra, R. M. Rowan-Robinson, A. Ciuculkaite, C. S. Davies, A. Dmitriev, V. Kapaklis, A. V. Kimel, A. Kirilyuk, *Nano Lett.* **2022**, *22*, 9773.
- [38] H. Zhu, M. Gao, C. Pang, R. Li, L. Chu, F. Ren, W. Qin, F. Chen, *Small Sci.* **2022**, *2*, 2100094.
- [39] A. Gabbani, G. Petrucci, F. Pineider, *J. Appl. Phys.* **2021**, *129*, 211101.
- [40] L. Uba, S. Uba, V. N. Antonov, *Phys. Rev. B* **2017**, *96*, 235132.
- [41] A. Ciuculkaite, <https://uu.diva-portal.org/smash/record.jsf?pid=diva2%3A1360280&dsid=4949>. (accessed: March 2024).
- [42] Y. Quessab, M. Deb, J. Gorchon, M. Hehn, G. Malinowski, S. Mangin, *Phys. Rev. B* **2019**, *100*, 024425.
- [43] G.-M. Choi, H. G. Park, B.-C. Min, *J. Magn. Mag. Mater.* **2019**, *474*, 132.
- [44] S. Alebrand, U. Bierbrauer, M. Hehn, M. Gottwald, O. Schmitt, D. Steil, E. E. Fullerton, S. Mangin, M. Cinchetti, M. Aeschlimann, *Phys. Rev. B* **2014**, *89*, 144404.
- [45] A. R. Khorsand, M. Savoini, A. Kirilyuk, A. V. Kimel, A. Tsukamoto, A. Itoh, T. Rasing, *Phys. Rev. Lett.* **2013**, *110*, 107205.
- [46] Z. Chen, S. Li, S. Zhou, T. Lai, *New J. Phys.* **2019**, *21*, 123007.
- [47] E. Turgut, C. La-O-Vorakiat, J. M. Shaw, P. Grychtol, H. T. Nembach, D. Rudolf, R. Adam, M. Aeschlimann, C. M. Schneider, T. J. Silva, M. M. Murnane, H. C. Kapteyn, S. Mathias, *Phys. Rev. Lett.* **2013**, *110*, 197201.
- [48] M. Berritta, R. Mondal, K. Carva, P. M. Oppeneer, *Phys. Rev. Lett.* **2016**, *117*, 137203.
- [49] Y. Liu, H. Cheng, P. Vallobra, H. Wang, S. Eimer, X. Zhang, G. Malinowski, M. Hehn, Y. Xu, S. Mangin, W. Zhao, *Appl. Phys. Lett.* **2023**, *122*, 022401.
- [50] A. Ceballos, A. Pattabi, A. El-Ghazaly, S. Ruta, C. P. Simon, R. F. L. Evans, T. Ostler, R. W. Chantrell, E. Kennedy, M. Scott, J. Bokor, F. Hellman, *Phys. Rev. B* **2021**, *103*, 024438.
- [51] V. López-Flores, N. Bergeard, V. Halté, C. Stamm, N. Pontius, M. Hehn, E. Otero, E. Beaurepaire, C. Boeglin, *Phys. Rev. B* **2013**, *87*, 214412.
- [52] M. D. Croitoru, S. V. Mironov, B. Lounis, A. I. Buzdin, *Adv. Quant. Technol.* **2022**, *5*, 2200054.
- [53] S. Mironov, A. Mel'nikov, I. Tokman, V. Vadimov, B. Lounis, A. Buzdin, *Phys. Rev. Lett.* **2021**, *126*, 137002.
- [54] B. J. Shastri, A. N. Tait, T. Ferreira De Lima, W. H. P. Pernice, H. Bhaskaran, C. D. Wright, P. R. Prucnal, *Nat. Photonics* **2021**, *15*, 102.